Nanoscale

Accepted Manuscript

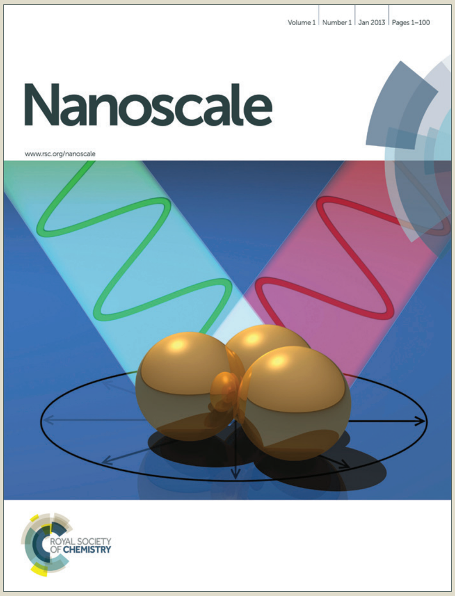

ROYAL SOCIETY OF CHEMISTRY

www.rsc.org/nanoscale

Nanoscale RSCPublishing

ARTICLE

Cite this: DOI: 10.1039/x0xx00000x

Received xxxx 2014,
Accepted xxxx 2014

DOI: 10.1039/x0xx00000x

www.rsc.org/Nanoscale

Porous $CuCo_2O_4$ Nanocubes wrapped by Reduced Graphene Oxide as High-Performance Lithium-Ion Battery Anodes

Wenpei Kang[a], Yongbing Tang[a,b]*, Wenyue Li[b,a], Zhangpeng Li[a], Xia Yang[a], Jun Xu[a] and Chun-Sing Lee[a]*

Composite of porous $CuCo_2O_4$ nanocubes well wrapped by reduced graphene oxide (rGO) sheets has been synthesized by a facile microwave-assisted solvothermal reaction and applied as anode in lithium ion batteries (LIBs). The porous structure of the $CuCo_2O_4$ nanocubes not only provides a high surface area for contacting with electrolyte, but also assists on accommodating volume change upon charging-discharging. Impedance measurements and transmission electron microscopy show that incorporation of rGO further decreases the charge transfer resistance and improves the structural stability of the composite. As anode material of LIB, the composite exhibits a high stable capacity of ~570 mAh g^{-1} at a current density of 1000 mA g^{-1} after 350 cycles. With a high specific surface area and a low charge transfer resistance, the composite anode shows impressive performance especially at high current density. The LIB shows a high capacity of ~450 mAh g^{-1} even at a high current density of 5000 mA g^{-1}, demonstrating the composite's potential for applications in LIBs with long cycling life and high power density.

1. Introduction

With increasing demand of high energy density storage for portable electronic devices, power tools, and electric vehicles, the development of high-performance lithium ion batteries (LIBs) with high specific energy is critically important.[1-3] However, the specific energy of conventional LIBs is not sufficient for these applications due to the limited specific capacity of the conventional graphite anode (372 mAh g^{-1}). Thus, exploration of new electrode materials with higher capacity is one of the most important research directions for LIB.[4-8] Transition-metal oxides (TMOs), especially cobalt-based oxides with a spinel structure, have been intensively investigated as possible alternatives to carbonaceous anode materials for their higher theoretical capacities.[9-18] In view of the high cost of Co, ternary cobalt oxides via partially substituting Co with less expensive metals, such as Ni, Zn, Fe, Mg, Cu, and Mn, etc.[19-25] are more practical anode materials for applications. Chowdari's group successfully introduced copper to partially replace cobalt to obtain a $CuCo_2O_4$ nanoparticle anode.[21] Copper is not only less expensive, but also electrochemically active and contribute to the charge storage. Their LIB delivers an impressive capacity of 745 mAh g^{-1} (after 20 cycles at a current rate of 60 mA g^{-1}) which is close to the theoretical capacity of 874 mAh g^{-1}. Reddy et al. have also reported a molten salt approach to synthesize $CuCo_2O_4$ nanoparticles, which has a dicharge capacity of ~740 mAh g^{-1} after 40 cycles.[24] Sun et al. obtained mesoporous $CuCo_2O_4$ structure by using porous silica as template, and the discharge capacity remains about 900 mAh g^{-1} after 6 cycles.[25] While the high capacities reported in these earlier works clearly suggested that $CuCo_2O_4$ has good potential for LIB application, several issues have to be addressed to enable its commercialization. For example, so far all reports on the $CuCo_2O_4$ anode use relatively low current densities (e.g. below 100 mA g^{-1}) and limited cycling numbers (<50 cycles) in the LIB characteriation.[21,24,25] Furthermore, the rate capability of reported $CuCo_2O_4$ anode need further optimization, because the capacity was found to decrease dramatically below 250 mAh g^{-1} when as the current density increased to 1 C (~800 mA g^{-1}).[25] Apparently, operation stability and high rating performance are two critical issues needing improvements, before wide application of $CuCo_2O_4$ can be realized.

Recent studies showed that the incorporation of graphene sheets can significantly improve the electrochemical performance of TMO composites.[26-37] Using graphene as conducting reinforcement, the cycling stability and rate capability of TMO anodes were enhanced due to the increased electrical conductivity and anode/electrolyte contact area. More recently, Sun's group demonstrated the preparation of a $CuCo_2O_4$ nanoparticles/reduced graphene oxide (rGO) composite, which exhibits a high efficiency of oxygen reduction.[38] Herein, we report a microwave-assisted solvothermal and calcination method for facile synthesis of porous $CuCo_2O_4$ nanocubes wrapped by graphene sheets for LIB application. The composite combine the advantages of porous nanostructure and graphene, in which the porous nanostructure provides fast three-dimensional Li^+ diffusion channels, and graphene sheets improve the conductivity and structural stability of the porous nanocubes. As anode of LIB, this composite exhibits a stable capacity of ~570 mAh g^{-1} at a current density of 1000 mA g^{-1} after 350 cycles. Moreover, it retains a capacity of ~450 mAh g^{-1} even at a high current density of 5000 mA g^{-1}, demonstrating its potential applications for LIBs with long cycling life and high power density.

2. Experimental

2.1 Preparation of Graphite Oxide (GO)

Uniform GO dispersion was prepared by a modified Hummers' method,[39] in which, graphite (3.0 g) was first pretreated in an 80°C solution of concentrated H_2SO_4 (12.0 mL), $K_2S_2O_8$ (2.5 g), and P_2O_5 (2.5 g) under stirring for 4.5 h. The mixture was then cooled to room temperature and diluted with de-ionized (DI) water, filtered, washed and dried. The pretreated graphite powder was then put into cold (0°C) concentrated H_2SO_4 (120.0 mL), followed by slowly adding 15.0 g of $KMnO_4$ under stirring below 20°C in an ice-water bath. The mixture was further stirred at 35°C for 12 h, and diluted with 750.0 mL DI water below 50°C. Then 30% H_2O_2 (20.0 mL) was added into the above mixture. At last the mixture was washed with sufficient HCl aqueous solution (5%) and DI water. The resulting GO was dispersed into the DI water under mild sonication to make a GO dispersion and the concentration is ~6 mg/mL.

2.2 Preparation of $CuCo_2O_4$/rGO composite

The $CuCo_2O_4$/rGO composite was prepared with a microwave-assisted solvothermal reaction followed by calcination treatment. In a typical process, 2.0 mL of the GO dispersion, 1.0 mmol $Co(CH_3COO)_2\cdot4H_2O$, 0.5 mmol $Cu(NO_3)_3\cdot3H_2O$ and 10.0 mmol CH_3COONa were dispersed into a solvent of 18.0 mL water and 20.0 mL triethylene glycol (TEG) under sonication. The above dispersion was sealed in a glass vessel and loaded into a microwave reactor, where the sample was heated with a microwave power of 50W at 170°C for 20 min. After cooling to room temperature, the precursor precipitate was collected by centrifugation, washed several times with DI water and ethanol, and dried at 70°C for 12 h. At last, the obtained precursor was calcinated at 600°C for 3 h under a N_2 atmosphere. In this process, the GO is partially reduced leading to the final $CuCo_2O_4$/reduced GO (rGO) composite. For comparison, a sample was also prepared without using GO.

2.3 Materials characterization

X-ray diffraction (XRD) measurements were carried out on a Siemens D-500 diffractometer with Cu Ka radiation. Scanning electron microscopy (SEM) and transmission electron microscopy (TEM) were respectively carried out with a Philips XL30 FEG SEM and a Philips FEG TEM CM200 (operated at 200 kV). Raman measurements were conducted with a Renishaw 2000 laser Raman microscope with a 633 nm argon ion laser. The specific surface areas of the samples were measured by nitrogen adsorption/desorption measurements using a Quantachrome NOVA-3000 system at 77 K. Thermogravimetric analyzer (TGA) measurement was performed under air atmosphere with a heating step of 10 °C min^{-1} from room temperature to 550°C.

2.4 Electrochemical measurements

Working electrodes were prepared by mixing the prepared samples with acetylene black and sodium carboxymethyl cellulose in a weight ratio of 7:2:1 with the weight loading of 2.1 ± 0.3 mg cm^{-2}. $LiPF_6$ solution (1 mol L^{-1}) in an ethylene carbonate and dimethyl carbonate mixture (1:1, v/v) was used as electrolyte. Lithium metal and Celgard 2025 (Celgard, Inc., USA) were respectively used as counter electrode and separator. CR2032-type coin cells were assembled in an argon-filled glove box. Galvanostatic cycling tests were measured using a Macco Instruments system. Cyclic voltammetry (CV) measurements were carried out over a potential window of 0-3.0 V with an electrochemical workstation (CHI 660D). Electrochemical impedance spectroscopy (EIS) was carried out on a ZAHNER-elektrik IM6 over a frequency range of 100 kHz to 5 mHz.

3. Results and Discussion

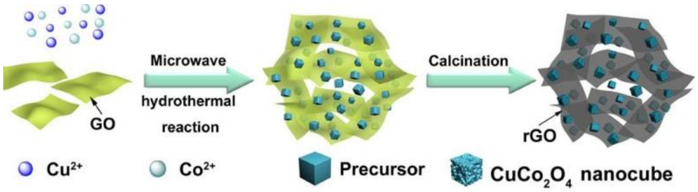

Fig. 1 Schematic diagram for the formation of porous $CuCo_2O_4$ nanocubes/rGO composite.

The preparation of the porous $CuCo_2O_4$ nanocubes/rGO composite is schematically illustrated in Fig. 1. Owing to the presence of oxygen-containing functional groups (e.g. hydroxyl etc) on the GO surface, Co^{2+} and Cu^{2+} ions can easily graft onto it by chemisorption. In the reaction mixture, sodium acetate will provide an alkaline environment favorable to the formation of metal oxide precipitates.[40-42] The addition of TEG decreases the polarity of the reaction medium and thus reduces the difference in the solubility of copper and cobalt salts. This would in turn favor the formation of a homogeneous $CuCo_2O_4$ precursor instead of a mixture of copper oxides and cobalt oxides. The microwave-assisted solvothermal reaction results in the formation of $CuCo_2O_4$ precursor on graphene oxide. Finally, upon calcination, organic residues are driven out of the $CuCo_2O_4$ precursor while the graphene oxide is partially reduced leaving behind the final product of a porous $CuCo_2O_4$ naoncubes/rGO composite.

As shown by XRD analysis, the precursor of the $CuCo_2O_4$/rGO composite contains a mixture of copper-cobalt oxide and copper-cobalt poly alcohol salt (Fig. S1a.) The copper-cobalt poly alcohol salt is always formed with in an alkaline environment under the solvothermal condition.[40-42] After calcination, the XRD patterns of the prepared samples are shown in Fig. 2a. The reflection peaks can be indexed to face-centered-cubic (fcc) $CuCo_2O_4$ (JCPDS NO 78-2177, a_0=0.8039 nm), indicating the formation of pure cubic phase $CuCo_2O_4$. It is generally suggested it adopts a spinel structure in which the copper atoms occupy the octahedral sites and cobalt atoms distribute over both octahedral and tetrahedral sites, as illustrated in Fig. S1b. The presence of rGO in the composite is confirmed by Raman spectroscopy as shown in Fig. 2b. The two peaks at 1336 and 1603 cm^{-1} belonging to the well documented D and G bands of rGO,[43] respectively, and the corresponding I_D/I_G ratio is 1.24, which is higher than that of GO (e.g. 0.90, Fig. S1c). This demonstrates that GO in the composite was reduced to rGO upon calcination. The rGO content is ~3% as determined with TGA analysis (Fig. S1d). Noted that the peaks of 475 and 492 cm^{-1} correspond to the Raman-active modes of Co-O,[44] and the marked peak (*) is from the Si substrate

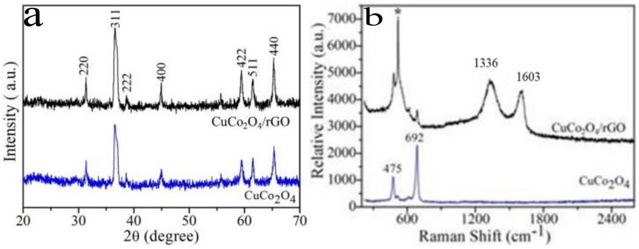

Fig. 2 (a) XRD patterns and (b) Ramman spectra of $CuCo_2O_4$/rGO and $CuCo_2O_4$.

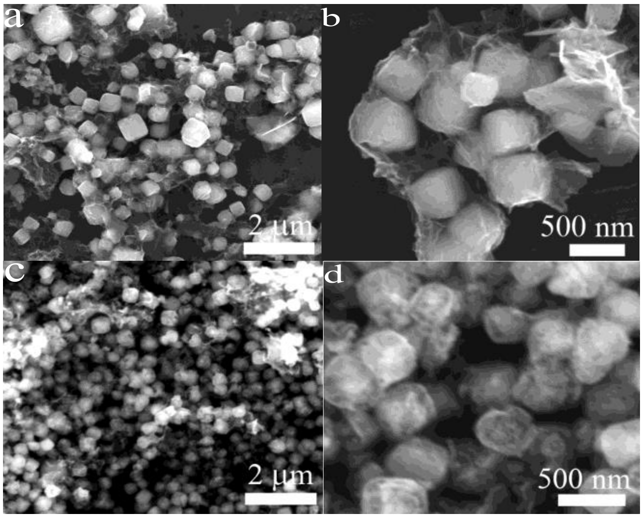

Fig. 3 SEM images of the $CuCo_2O_4$ nanocubes/GO precursor (a, b) and porous $CuCo_2O_4$ nanocubes/rGO composite (c, d).

An SEM image (Fig. 3a) shows that the $CuCo_2O_4$/GO precursor consists of many nanoparticles with several hundreds of nanometer size. It can be seen from a high magnification image (Fig. 3b) that the nanoparticles have a cube-like morphology and are wrapped by GO sheets. Pristine $CuCo_2O_4$ precursor nanoparticles with a similar cubic morphology (Fig. S2a, b) were also formed if GO is not used in the reactants. After calcination at 600°C, the precursors transformed into porous $CuCo_2O_4$ nanocubes, as shown in Fig. 3c and d, which should be resulted from the decomposition of metal glycolates in the precursor. Similarly, the pristine $CuCo_2O_4$ nanocubes without GO also develops a porous structure upon heat treatment (Fig. S2c, d). To further determine the composition and uniformity, energy dispersive X-ray (EDX) elemental mapping was performed for the porous $CuCo_2O_4$ nanocubes/rGO composite. A typical EDX spectrum (Fig. S3) verifies that the as-prepared composite is indeed composed of Cu, Co, and O, as well as uniformly distributed C.

Microstructure of the as-synthesized composite was further investigated with transmission electron microscopy (TEM) as shown in Fig. 4. It can be obviously seen that porous $CuCo_2O_4$ nanocubes are well wrapped by rGO sheets (Fig. 4a). Meanwhile, the porous feature of the nanocubes is further shown in Fig. 4b. Fig. 4c is a representative high-resolution TEM (HRTEM) image of a single $CuCo_2O_4$ nanocube. The interplanar spacing of 0.28 nm corresponds to the (220) plane of the cubic spinel $CuCo_2O_4$. A corresponding selected area electron diffraction (SAED) pattern (Fig. 4d) can be indexed to (220) and (400) planes, which is consistent with the HRTEM observation. On the other hand, the prepared $CuCo_2O_4$ sample, without using GO, also has a single-crystalline nature with a spinel structure (Fig. S4).

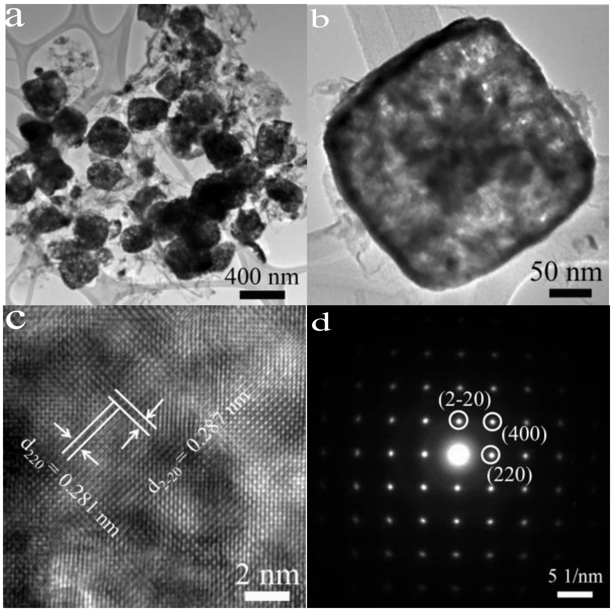

Fig. 4 TEM image (a, b), HR TEM image (c), and SAED pattern (d) of porous $CuCo_2O_4$ nanocubes/rGO composite.

Specific surface areas of the as-prepared samples were investigated by nitrogen adsorption/desorption measurements. Brunauer-Emment-Teller (BET) analyses of the porous $CuCo_2O_4$ nanocubes/rGO composite and the pristine $CuCo_2O_4$ nanocubes (Fig. S5a and b) gives specific surface areas of 34.4 and 10.9 m^2g^{-1}, respectively. Comparing with bulk $CuCo_2O_4$, the high specific surface area of the porous nanostructures substantially increase their contact areas with the electrolyte solution when applied as LIB anodes.

Fig. 5 shows CV curves of the electrodes composed of the porous $CuCo_2O_4$ nanocubes/rGO composite and the pristine $CuCo_2O_4$ nanocubes at a scan rate of 0.2 mV s^{-1} over a potential window of 0.0–3.0 V. In the first cathodic process of the $CuCo_2O_4$/rGO composite, two reduction peaks can be found (Fig. 5a). The weak peak located at about ~0.88 V can be attributed to the reduction of Co^{3+} to Co^{2+}, and the intense peak at ~0.50 V could be assigned to the further reduction of Co^{2+} or

Cu^{2+} to metallic Co or Cu; In the corresponding anodic sweep, there is an oxidation peak at ~2.11 V corresponding to the oxidation of Co to Co^{2+} and Cu to Cu^{2+}.[25] In the following 2nd and 10th cycles, it can be observed that the reduction peak is moved to ~1.15 V and ~0.96 V and the oxidation peak moved to ~2.15 V. For the pristine $CuCo_2O_4$ electrode, the redox peaks are similar to those of the $CuCo_2O_4$/rGO electrode (Fig. 5b). In the first cathodic process, the reduction peaks shift to high potential and only one reduction peak can be found attributed to the electrode polarization, and the peak at 0.31 V is due to the formation of solid electrolyte interface (SEI) layers.[45] In addition, the intensity of the redox peaks decrease gradually along the cycling process, indicating that the discharge-charge capacity of the $CuCo_2O_4$ is likely to be less stable.

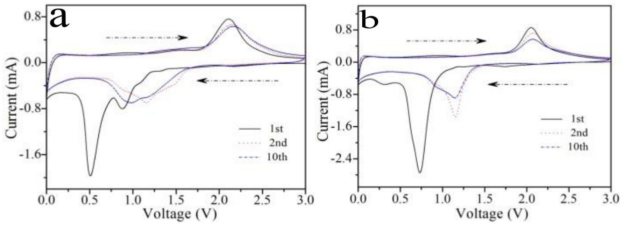

Fig. 5 CV curves of (a) $CuCo_2O_4$/rGO composite and (b) pristine $CuCo_2O_4$ at a scan rate of 0.2 mV s^{-1} between 0.0-3.0 V.

Long-term cycling performances of the porous $CuCo_2O_4$ nanocubes/rGO composite and the pristine $CuCo_2O_4$ nanocubes were measured and compared at high current densities of 1.0 and 2.0 A g^{-1}. Fig. S6a, b shows representative discharge-charge profiles of $CuCo_2O_4$/rGO composite and pristine $CuCo_2O_4$ electrodes at a current density of 1 A g^{-1} (0.01 – 3.0 V), which are consistent with CV measurements. Relationships of specific discharge capacity versus cycle number are shown in Fig. 6a. It is interesting to observe that the discharge capacity of the composite increased considerably in the initial 80 cycles. At a current density of 1.0 A g^{-1}, the discharge capacity is ~540 mAh g^{-1} at the 2nd cycle, while this value increases to 721 mAh g^{-1} at the 80th cycle. This initial capacity increase is attributed to the gradual activation of the electrode.[46-48] After that, the capacity decreases from ~720 mAh g^{-1} to 577 mAh g^{-1} within 180 cycles with a high coulombic efficiency of ~99%. From the 180th cycle upwards, the capacity show relative mild change and the discharge capacity is 572 mAh g^{-1} after 350 cycles, which is much higher than the theoretical maximum of graphite (i.e. 372 mAh g^{-1}). Moreover, at a higher current density of 2.0 A g^{-1} the discharge capacity of the composite also shows a similar variation trend and maintain an impressive value of 471.7 mAh g^{-1} after 350 cycles.

Noted that the phenomenon of the gradually increased capacity in the initial tens of cycles is normally observed for TOMs, which is attributed to the reversible formation of a polymeric gel-like film originating from kinetic activation in the electrode.[49] Additionally, the porous structures and conductive substrate rGO are another important factors for the increasing capacities.[50,51] There is a long active period for the electrolyte penetrating into the inner part of the porous $CuCo_2O_4$ nanocubes/rGO composite, making the inner part also involved in the conversion reactions, which results in an increased capacities in the initial cycles. However, as the redox reaction proceeding, the microstructure might change and lead to gradual capacity fading. To study the effect of rGO, the cycling performance of the pristine $CuCo_2O_4$ nanocubes was also evaluated (Fig. 6a). At the same current density of 1.0 or 2.0 A g^{-1} the discharge capacity decrease gradually in the initial 50 cycles. Afterwards, the capacities are almost stable and in the 350th cycle can keep at 298.1 and 250.6 mAh g^{-1} at 1.0 or 2.0 A g^{-1}, respectively. It is clear that the rate capability and cycle stability of the porous $CuCo_2O_4$ nanocubes/rGO composite are significantly enhanced by the rGO.

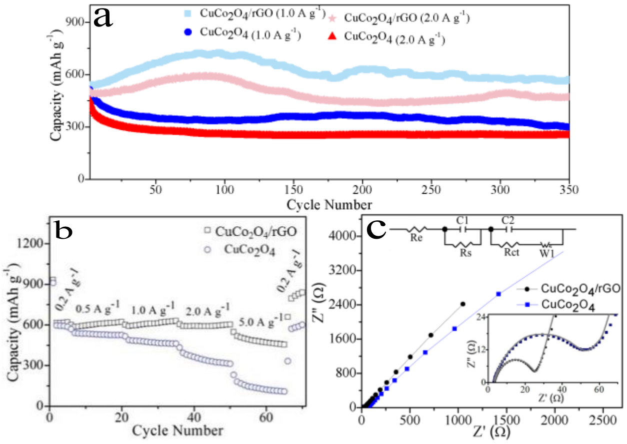

Fig. 6 (a) Cycling performance from 2 to 350 cycles, (b) Rate capability, and (c) Nyquist plots in the range of 100 kHz to 5 mHz of $CuCo_2O_4$/rGO composite and pristine $CuCo_2O_4$ electrodes, and the insets in the panel (c) are the equivalent circuit and the fitted curves.

Rate performances of the porous $CuCo_2O_4$ nanocubes/rGO composite and the pristine $CuCo_2O_4$ nanocubes were measured and compared (Fig. 6b). Upon cycling at current densities of 0.2, 0.5, 1.0, 2.0 and 5.0 A g^{-1}, the LIB with the porous $CuCo_2O_4$ nanocubes/rGO electrode shows discharge capacities of 620, 621, 629, 603 and 454 mAh g^{-1} respectively. The corresponding capacities of the LIB with the pristine $CuCo_2O_4$ nanocube anode are 586, 526, 461, 313, 108 mAh g^{-1} respectively. Obviously, the composite exhibits much better rate capacity than the pristine $CuCo_2O_4$ nanocubes. Both samples regain their initial capacities at a current density of 0.2 A g^{-1} after the rate testing, suggesting good rate-cycling stability for the anodes.[46] Moreover, when the $CuCo_2O_4$/rGO electrode cycled at low current of 0.2 A g^{-1}, within the 100 cycles the capacities increase continuously as show in Fig. S6. It can be noted from figure 6b that the composite shows slightly higher capacities as the current density increases and that the final capacity at 0.2 A g^{-1} is higher than the initial capacity at 0.2 A g^{-1}. These can be explained by the capacity increase during the activation of the composite anode (Fig. 6a and S6). The rate capacity of porous $CuCo_2O_4$ nanocubes/rGO composite in this work is better than those of previously reported nano-phase $CuCo_2O_4$ structures (380 mAh g^{-1} at current of 750 mA g^{-1}) and mesoporous crystalline $CuCo_2O_4$ (246 mAh g^{-1} at current of 800 mA g^{-1}),[21,25] and this composite exhibits better or comparable rate capability and cycle stability compared with other binary transition metal oxides (Table S1).[52-54] This should be attributed to the rGO sheets provide a highly conductive medium for electron transfer during the lithiation/de-lithiation process. Meanwhile, the porous framework of nanocubes not only allows efficient active mass-electrolyte contact but also better accommodates the strains related to volume changes upon repeated Li^{+} insertion/extraction.

We carried out electrochemical impedance spectroscopy (EIS) measurements over the frequency range from 5 mHz to 100 kHz to investigate charge transfer mechanisms of the porous $CuCo_2O_4$ nanocubes/rGO composite in LIBs. Typical Nyquist plots of the cells with the composite and the $CuCo_2O_4$ nanocube electrodes are shown in Fig. 6c. All the plots exhibit a semicircle in the high frequency region and a straight line in the low-frequency region. An intercept at the Z' axis in high frequency is related to the resistance of the electrolytes (R_s). The semicircle in the middle frequency range corresponds to the charge-transfer resistance (R_{ct}), indicating the charge transfer through the electrode/electrolyte interface. From the Nyquist plot, R_{ct} for the porous $CuCo_2O_4$ nanocubes/rGO composite and the $CuCo_2O_4$ nanocubes were determined to be ~15 and ~31 Ω, respectively. The results indicated that rGO can effectively decrease the charge transfer resistance and thus facilitates charge-transfer in the LIBs.

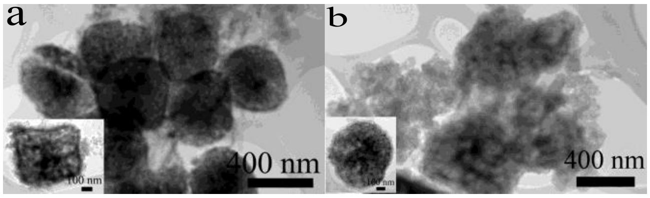

Fig. 7 TEM images of (a) $CuCo_2O_4$/rGO composite and (b) pristine $CuCo_2O_4$ electrode after long-term cycling at the current density of 2.0 A g^{-1}.

To understand the relationship between the improved performances and structure, we study the morphology changes of the porous $CuCo_2O_4$ nanocubes/rGO electrode upon cycling. Fig. 7 shows TEM images of the porous $CuCo_2O_4$ nanocubes/rGO and the pristine $CuCo_2O_4$ nanocube electrodes after 350 cycles. It can be seen that the composite basically maintains its original microstructure (Fig. 7a) with porous cubic crystals (inset of Fig. 7a) wrapped with graphene. On the other hand, the pristine $CuCo_2O_4$ electrode shows more obvious microstructure changes (Fig. 7b). In particular, the cubic crystals become more rounded and appear to be more porous. It is considered that the presence of the reduced graphene oxide can accommodate part of the volume changes in the active material and act as a buffer reagent, resulting in improved cycling performance. These results illustrate that the combination of reduced graphene oxide with porous $CuCo_2O_4$ nanocubes can indeed optimize the morphology stability of the porous $CuCo_2O_4$ nanocubes, which results in the improved cycling stability and rate capacity of the electrode material.

4. Conclusions

In summary, we have developed a scalable microwave-assisted solvothermal method for facile synthesis of porous $CuCo_2O_4$ nanocubes/rGO composite. As anode for LIBs, this composite exhibits a high cycling stability and rate capability. The discharge capacity of the composite is about 570 mAh g^{-1} at a current of 1.0 A g^{-1} after 350 cycles, which is much higher than the reported results for $CuCo_2O_4$ at similar current rate.[21,25] Especially, even at a high current of 5.0 A g^{-1} the discharge can also retain 450 mAh g^{-1}, indicating a good rate capacity. The high performance is resulted from the fact that the composite simultaneously combines the advantages of porous structure and rGO. The porous structure provides sufficient contact with electrolyte and fast three-dimensional Li^+ diffusion channels; meanwhile, rGO improves the conductivity and structural stability of the porous nanocubes during the insertion/extraction of Li^+. It is believed that the scalable preparation process and high electrochemical performance of the porous $CuCo_2O_4$ nanocubes/rGO composite would pave the way for its practical LIB application.

Acknowledgements

This project has been financially supported by National Natural Science Foundation of China (Nos. 51272217, 51302238), Collaboration Project of City University of Hong Kong and Shenzhen Huawei (YB2012090343).

Notes and references

a Department of Physics and Materials Science and Center of Super-Diamond and Advanced Films (COSDAF), City University of Hong Kong, Hong Kong SAR, People's Republic of China.

b Functional Thin Films Research Center, Shenzhen Institutes of Advanced Technology, Chinese Academy of Sciences, People's Republic of China.

*Corresponding author.

E-mail: tangyb@siat.ac.cn; apcslee@cityu.edu.hk; Tel: +852-34427826

Electronic Supplementary Information (ESI) available: [details of any supplementary information available should be included here]. See DOI: 10.1039/b000000x/

1 M. V. Reddy, G. V. Subba Rao, and B. V. R. Chowdari, *Chem. Rev.*, 2013, **113**, 5364.

2 L. G. Lu, X, B, Han, J. Q. Li, J. F. Hua and M. G. Ouyang. *J. Power Sources*, 2013, **226**, 272.

3 J. Liu, J. G. Zhang, Z.G. Yang, J. P. Lemmon, C. Imhoff, G. L. Graff , L. Y. Li, J. Z. Hu, C.M. Wang, J. Xiao, G. Xia, V. V. Viswanathan, S. Baskaran, V. Sprenkle, X. L. Li, Y. Y. Shao and B. Schwenzer, *Adv. Funct. Mater.*, 2013, **23**, 929.

4 P. Poizot, S. Laruelle, S. Grugeon, L. Dupont and J. M. Tarascon *Nature*, 2000, **407**, 496.

5 L.W. Ji, Z. Lin, M. Alcoutlabi and X.W. Zhang, *Energy Environ. Sci.*, 2011, **4**, 2682.

6 Y. G. Wang, H. Q. Li, P. He, E. Hosono and H. S. Zhou, *Nanoscale*, 2010, **2**, 1294.

7 A. Manthiram, A. Vadivel Murugan, A. Sarkar and T. Muraliganth, *Energy Environ. Sci.*, 2008, **1**, 621.

8 F. Y. Cheng, J. Liang, Z. L. Tao and J. Chen, *Adv. Mater.*, 2011, **23**, 1695.

9 H. B. Wu, J. S. Chen, H. H. Hong and X. W. Lou, *Nanoscale*, 2012, **4**, 2526.

10 L. Zhou, D. Y. Zhao and X. W. Lou, *Adv. Mater.*, 2012, **24**, 745.

11 J. X. Zhu, Z. Y. Yin, D. Yang, T. Sun, H. Yu, H. E. Hoster, H. H. Hng, H. Zhang and Q. Y. Yan, *Energ. Environ. Sci.*, 2013, **6**, 987.

12 M. X. Li, Y. X. Yin, C. J. Li, F. Z. Zhang, L. J. Wan, S. L. Xu and D. G. Evans, *Chem. Commun.*, 2012, **48**, 410.

13 E. Vila, R. M. Rojas, J. L. M. Vidales and O. G. Martinez, *Chem. Mater.*, 1996, **8**, 1078.

14 T. Y. Wei, C. H. Chen, H. C. Chien, S. Y. Lu and C. C. Hu, *Adv. Mater.*, 2010, *22*, 347.

15 W. Y. Li, L. N. Xu and J. Chen, *Adv. Funct. Mater.*, 2005, **15**, 851.

16 Z. S. Wu, W. C. Ren, L. Wen, L. B. Gao, J. P. Zhao , Z. P. Chen, G. M. Zhou, F. Li and H. M. Cheng, *ACS Nano*, 2010, **4**, 3187.

17 C. Z. Yuan, H. B. Wu, Y. Xie, and X. W. Lou, *Angew. Chem. Int. Ed.*, 2014, **53**, 1488.

18 Z. Y. Wang, Z. C. Wang, W. T. Liu, W. Xiao and X. W. Lou *Energy Environ. Sci.*, 2013, **6**, 87.

19 R. Alcántara, M. Jaraba, P. Lavela and J. L. Tirado, *Chem. Mater.*, 2002, **14**, 2847.

20 L. L. Hu, B. H. Qu, C. C. Li, Y. J. Chen, L. Mei, D. N. Lei, L. B. Chen, Q. H. Li and T. H. Wang, *J. Mater. Chem. A*, 2013, **1**, 5596.

21 Y. Sharma, N. Sharma, G. V. S. Rao and B. V. R. Chowdari, *J. Power Sources*, 2007, **173**, 495.

22 J. F. Li, S. L. Xiong, X. W. Li and Y. T. Qian, *Nanoscale*, 2013, **5**, 2045.

23 Y. Sharma, N. Sharma, G.V. Subba Rao and B.V. R. Chowdari, *Solid State Ionics*, 2008, **179**, 587.

24 M. V. Reddy, Y. Cai, J. H. Fan, K. P. Loh and B. V. R. Chowdari, *RSC Adv.*, 2012, **2**, 9619.

25 S. J. Sun, Z. Y. Wen, J. Jin, Y. M. Cui, and Y. Lu, *Micropor. Mesopor. Mater.*, 2013, **169**, 242.

26 H. L. Wang, L. F. Cui, Y. Yang, H. S. Casalongue, J. T. Robinson, Y. Y. Liang, Y. Cui and H. J. Dai. *J. Am. Chem. Soc.*, 2010, **132**, 13978.

27 G.M. Zhou, D. W. Wang, F. Li, L. L. Zhang, N. Li, Z. S. Wu, L. Wen, G. Q. Lu and H. M. Cheng. *Chem. Mater.*, 2010, **22**, 5306.

28 L. Li, A. R. O. Raji and J. M. Tour, *Adv. Mater.*, 2013, **25**, 6298.

29 J. X. Zhu, T. Zhu, X. Z. Zhou, Y. Y. Zhang, X. W. Lou, X. D. Chen, H. Zhang, H. H. Hng and Q. Y. Yan, *Nanoscale*, 2011, **3**, 1084.

30 Y. Q. Zou and Y. Wang, *Nanoscale,* 2011, **3**, 2615.

31 J. S. Chen, Z. Y. Wang, X. C. Dong, P. Chen and X. W. Lou, *Nanoscale,* 2011, **3**, 2158.

32 K. K. Lee, S. Deng, H. M. Fan, S. Mhaisalkar, H. R. Tan, E. S. Tok, K. P. Loh, W. S. Chin and C. H. Sow, *Nanoscale,* 2012, **4**, 2958.

33 B. G. Choi, S. J. Chang, Y. B. Lee, J. S. Bae, H. J. Kim and Y. S. Huh, *Nanoscale*, 2012, **4**, 5924.

34 F. Zhang, T. F. Zhang, X. Yang, L. Zhang, K. Leng, Y. Huang and Y. S. Chen, *Energy Environ. Sci.*, 2013, **6**, 1623.

35 X. S. Zhou, L. J. Wan and Y. G. Guo, *Adv. Mater.*, 2013, **25**, 2152.

36 B. Wang, X. L. Wu, C. Y. Shu, Y. G. Guo and C. R. Wang, *J. Mater. Chem.*, 2010, **20**, 10661.

37 D. Wang, J. Yang, X. Li, D. Geng, R. Li, M. Cai, T. K. Sham and X. Sun, *Energy Environ. Sci.*, 2013, **6**, 2900.

38 R. Ning, J. Q. Tian, A. M. Asiri, A.H. Qusti, A. O. Al-Youbi, and X. P. Sun, *Langmuir*, 2013, **29**, 13146.

39 Y. X. Xu, H. Bai, G. W. Lu, C. Li and G. Q. Shi, *J. Am. Chem. Soc.*, 2008, **130**, 5856.

40 A. M. Cao, J. D. Monnell, C. Matranga, J. M. Wu, L. L. Cao and D. Gao, *J. Phys. Chem. C*, 2007, **111**, 18624.

41 Y. L. Wang, X. C. Jiang and Y. N. Xia, *J. Am. Chem. Soc.*, 2003, **125**, 16176.

42 Y. C. Qiu, S. H. Yang, H. Deng, L. M. Jin and W. S. Li, *J. Mater. Chem.*, 2010, **20**, 4439.

43 N. Li, Z. F. Geng, M. H.a Cao, L. Ren, X. Y. Zhao, B. Liu, Y. Tian and C. W. Hu, *Carbon*, 2013, **54**, 124.

44 Q. Z. Jiao, M. Fu, C. You, Y. Zhao and H. S. Li, *Inorg. Chem.*, 2012, **51**, 11513.

45 W. P. Kang, F. L. Liu, Y. L. Su, D. J. Wang and Q. Shen, *CrystEngComm*, 2011, **13**, 4174.

46 C. X. Peng, B. D. Chen, Y. Qin, S. H. Yang, C. Z. Li, Y. H. Zuo, S. Y. Liu and J. H. Yang, *Acs Nano*, 2012, **6**, 1074.

47 W. P. Kang and Q. Shen, *J. Power Sources*, 2013, **238**, 203.

48 M. Kundu, C. C. Albert Ng, D. Y. Petrovykh and L. F. Liu, *Chem. Commun.*, 2013, **49**, 8459.

49 J. S. Do and C. H. Weng, *J. Power Sources*, 2005, **146**, 482.

50 J. F. Li, S. L. Xiong, X. W. Li and Y. T. Qian, *J. Mater. Chem.*, 2012, **22**, 23254.

51 J. F. Li, S. L. Xiong, Y. R. Liu, Z. C. Ju and Y. T. Qian, *ACS Appl. Mater. Interfaces*, 2013, **5**, 981.

52 D. Q Liu, Xi Wang, X. B. Wang, W. Tian, Y. Bando and D.Golberg, *Sci. Rep.*, 2013, **3**, 2543.

53 X. L. Xiao, X. F. Liu, H. Zhao, D. F. Chen, F. Z. Liu, J. H. Xiang, Z. B. Hu and Y. D. Li, *Adv. Mater.*, 2012, **24**, 5762.

54 S. L. Xiong, J. S. Chen, X. W. Lou and H. C. Zeng, *Adv. Funct. Mater.*, 2012, **22**, 861.